PHOTONICS Research

All-angle optical switch based on the zero reflection effect of graphene–dielectric hyperbolic metamaterials

Wenyao Liang,[1,*] Zheng Li,[2] Yu Wang,[1] Wuhe Chen,[1] and Zhiyuan Li[1]

[1]School of Physics and Optoelectronics, South China University of Technology, Guangzhou 510640, China
[2]School of Electronic and Information Engineering, South China University of Technology, Guangzhou 510640, China
*Corresponding author: liangwenyao@scut.edu.cn

Received 18 October 2018; revised 8 January 2019; accepted 21 January 2019; posted 23 January 2019 (Doc. ID 348666); published 25 February 2019

We have studied a switchable hyperbolic metamaterial composed of a graphene–dielectric periodic structure. By tuning the chemical potential of all graphene sheets simultaneously, the isofrequency curve can switch between an ellipse and a hyperbola conveniently. In particular, a special hyperbolic isofrequency curve with its asymptote perpendicular to the interface is obtained and used to realize the zero reflection effect. Furthermore, a zero-reflection-based optical switch working in the terahertz spectrum is demonstrated. Its bandwidth can be efficiently adjusted by geometric parameters such as permittivity and period. Such an optical switch possesses the merits of low loss, high transmittance contrast, high response speed, compact size, high tolerance of chemical potential, and having all incident angles (0°–90°) simultaneously. Such an optical switch holds great potential in many fields, such as data storage, beam steering, and integrated photonic circuits. © 2019 Chinese Laser Press

https://doi.org/10.1364/PRJ.7.000318

1. INTRODUCTION

Metamaterials, which are artificial subwavelength structured materials, have been a hot topic of central importance due to their properties never observed in nature [1–3]. Among them, hyperbolic metamaterials are one of the most unusual classes of metamaterials [4,5]. Hyperbolic metamaterials have a diagonal permittivity tensor (or permeability tensor) whose principal components possess opposite signs. This special feature leads to its unusual hyperbolic dispersion and many unique properties. Unlike conventional double-negative metamaterials realized by a resonant-mediated mechanism, hyperbolic metamaterials not only simplify structures, but also make tunability possible. Hyperbolic metamaterials have attracted growing attention recently, whose applications involve negative refraction [6–8], nano-scale waveguides [9,10], sub-wavelength imaging [11], and spontaneous emission [12,13].

Metal is the most common material used to fabricate hyperbolic metamaterials, and the most common structures are nanowire-array structures [14] and layered metal–dielectric structures [15]. For example, the zero reflection effect in a metal–dielectric metamaterial was studied [16]. However, an inherent problem of such a metal-structured composite is material loss. Moreover, it is difficult to control the permittivity of metals after fabrication. Overcoming these two drawbacks is highly desired. Magnetic metamaterial based on YIG–dielectric layered structure is another kind of hyperbolic metamaterial, and it is used for optical switch design [17]; however, its modulation speed is low, and it works only in the microwave spectrum, since it does not have a magnetic response in infrared and terahertz spectra. What is more, it requires a bulky magnetic field unit for control, which is not convenient for practical applications and is unfavorable for miniaturization. In contrast to metal, graphene, a one-atom-thick allotrope of carbon first discovered in 2004 [18], is lossless and has excellent electronic and optical properties in infrared and terahertz spectra. Furthermore, its dielectric permittivity can be tuned by chemical potential, Fermi energy, external electrostatic field biasing, gate voltage, magnetic field, chemical doping, or the nonlinear effect [19–24], so graphene is a good candidate for overcoming the aforementioned drawbacks of metal and can work in infrared and terahertz spectra, which is favorable for on-chip integration. Recently, multilayer structures consisting of graphene and dielectric have been studied as tunable hyperbolic metamaterials [25–29]. The topological transitions and associated ultrafast optical properties in graphene-based hyperbolic metamaterials were studied [30–32]. Later, it was revealed that a surface wave exists at the interface between two different hyperbolic metamaterials, and the corresponding frequency ranges of the surface wave can be tuned by changing the Fermi energy of graphene sheets [24]. Graphene-based metamaterials have been used to realize negative refraction [6–8], modulators [33], meta-lenses [34], absorbers [35–37], vortex

waves [38], waveguides [9,10,25], and optical switches [39,40]. Very recently, a structure consisting of Kerr metallic nanolayers and graphene sheets was proposed to design an optical switch [41], but this metal–graphene structure has a complicated five-layer unit cell and inevitably introduces absorption loss, requiring high fabrication techniques and limiting the performance of the optical switch. From the view of applications, it is highly desired to develop a new mechanism to realize an optical switch that can overcome all the above-mentioned disadvantages, such as material loss, low response speed, and a bulky magnetic control unit, simultaneously.

In this work, we study a graphene–dielectric switchable hyperbolic metamaterial (SHM) and tune its effective permittivity by graphene's chemical potential. In this way, the isofrequency curve (IFC) of the SHM can switch between ellipse and hyperbola conveniently. When the asymptote of the hyperbolic IFC is perpendicular to the SHM–air interface, there is no reflected wave for any incident angles from the SHM, i.e., the zero reflection effect occurs. Furthermore, by using the peculiar and excellent opto-electronic properties of graphene, an all-angle (0°–90°) optical switch based on the zero reflection effect is demonstrated. Such an optical switch possesses low loss, high transmittance contrast, high response speed, compact size, and high tolerance of chemical potential simultaneously. Additionally, its working frequency range can be adjusted by geometric parameters.

2. ALL-ANGLE ZERO REFLECTION OPTICAL SWITCH

A. Analysis of Graphene–Dielectric Stacking Metamaterials

The schematic of the optical switch based on SHM is depicted in Fig. 1(a). The SHM is constructed by stacking monolayer graphene sheets with surface conductivity $\sigma(f)$ and dielectric layers with permittivity ε_d alternatively along the z axis with a period $d = 0.1$ μm. ε_d is adopted to be 2.2, which was used in Ref. [25]. The SHM and air are above and below the interface, respectively. The SHM is truncated at a slanted angle α with respect to the x axis.

Graphene is a very thin material layer with a thickness as small as one atom, which is very small compared with the period d of the SHM. Moreover, it has extremely high carrier mobility of $15,000\ \mathrm{cm^2/(V\cdot s)}$, which theoretically makes an optical switch with high response speed on the order of ps possible [42]. In our study, graphene is modeled as a two-dimensional surface and characterized by using a surface conductivity rather than a volumetric permittivity. The surface conductivity of graphene can be calculated by the Kubo formula [19,43]:

$$\sigma(f,\mu_c,\Gamma,T)=\frac{ie^2k_BT}{2\pi\hbar^2(\pi f+i\Gamma)}\left[\frac{\mu_c}{k_BT}+2\ln(e^{-\mu_c/k_BT}+1)\right]+\frac{i2e^2(\pi f+i\Gamma)}{\pi\hbar^2}\int_0^{\infty}\mathrm{d}\epsilon\frac{f_d(-\epsilon)-f_d(\epsilon)}{4(\pi f+i\Gamma)^2-4(\epsilon/\hbar)^2},\tag{1}$$

where e is the charge of an electron, k_B is the Boltzmann's constant, $\hbar$ is the reduced Planck constant, $f_d(\epsilon)=\{1+\exp[(\epsilon-\mu_c)/(k_BT)]\}^{-1}$ is the Fermi–Dirac distribution, ϵ is the energy, f is the frequency, and μ_c is the chemical potential determined by the carrier density n_s. $\Gamma = 0.1$ meV is the phenomenological scattering rate. $T = 300$ K is the temperature. The above surface conductivity material function is available in the material database in finite-difference time-domain (FDTD) software.

To realize the optical switch to be discussed later, the chemical potential of all graphene sheets needs to be changed simultaneously. The chemical potential depends on the carrier density and can be controlled by its chemical potential, external electrostatic field biasing, gate voltage, magnetic field, chemical doping, or nonlinear effect [19–22]. For example, one effective way to do this is by using external electrostatic field biasing E_{bias}. The relation between E_{bias} and μ_c is deduced as [18,19]

$$E_{\mathrm{bias}}=\frac{2e}{\pi\hbar^2v_F^2\varepsilon_0\varepsilon_d}\left[(k_BT)^2\int_{-\mu_c/k_BT}^{\mu_c/k_BT}\frac{x}{e^x+1}\mathrm{d}x+k_BT\mu_c\ln(e^{-\mu_c/k_BT}+1)+k_BT\mu_c\ln(e^{\mu_c/k_BT}+1)\right],\tag{2}$$

where $v_F\approx 9.5\times10^5$ m/s is the Fermi velocity, and ε_0 is the permittivity of free space. The other parameters are the same as those in Eq. (1).

In the THz spectrum, the period d of the structure is far less than the working wavelength. So the designed SHM can be modeled as a homogenous uniaxial anisotropic medium by the effective medium approximation method. The diagonal elements of effective relative permittivity tensor $\varepsilon_{\mathrm{eff}}$ of the SHM is described as $\{\varepsilon_{\parallel},\varepsilon_{\parallel},\varepsilon_{\perp}\}$ and given as follows [44]:

$$\varepsilon_{\perp}=\varepsilon_d,\varepsilon_{\parallel}=\varepsilon_d-i\frac{\sigma(\omega,\mu_c,\Gamma,T)}{\omega\varepsilon_0 d},\tag{3}$$

where $\parallel$ and $\perp$ denote the components parallel and perpendicular to the graphene sheets.

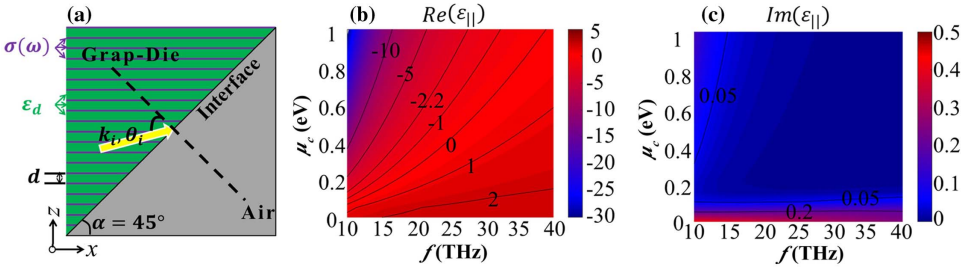

Fig. 1. (a) Schematic of the zero-reflection-based optical switch; the period of the SHM is d. (b), (c) $\mathrm{Re}(\varepsilon_{\parallel})$ and $\mathrm{Im}(\varepsilon_{\parallel})$ as functions of frequency and chemical potential.

From Eq. (3), one knows that $\varepsilon_\perp$ is a constant equal to the permittivity of dielectric layers, while $\varepsilon_\parallel$ is complex, depending on frequency f and chemical potential μ_c. By combining Eqs. (1) and (3), $\mathrm{Re}(\varepsilon_\parallel)$ and $\mathrm{Im}(\varepsilon_\parallel)$ are calculated and shown in Figs. 1(b) and 1(c). In Fig. 1(b), one can see that $\mathrm{Re}(\varepsilon_\parallel)$ decreases as μ_c increases or f decreases. Moreover, the value of $\mathrm{Re}(\varepsilon_\parallel)$ can cross the threshold of zero by tuning μ_c in a wide frequency range. In Fig. 1(c), one can see that $\mathrm{Im}(\varepsilon_\parallel)$ is small enough to be neglected as compared with $\mathrm{Re}(\varepsilon_\parallel)$ when $\mu_c \geq 0.2$ eV.

B. Realization of the All-Angle Zero-Reflection-Based Optical Switch

As depicted in Fig. 1(a), a Gaussian beam with waist width of 10 μm is incident from the SHM to air at an incident angle θ_i. Due to the symmetry of the 1D periodic structure, only the x–z section needs to be considered. The simplified dispersion relation of extraordinary waves (TM waves) is given as

$$\frac{k_x^2}{\varepsilon_\perp} + \frac{k_z^2}{\varepsilon_\parallel} = k_0^2, \tag{4}$$

where $k_0 = 2\pi f(\mu_0\varepsilon_0)^{1/2}$ is the wavenumber in vacuum. $\varepsilon_\perp$ is positive and cannot be tuned after fabrication. $\varepsilon_\parallel$ is a complex number depending on f and μ_c. However, Figs. 1(b) and 1(c) imply that $\varepsilon_\parallel$ is approximate to a real number due to its tiny $\mathrm{Im}(\varepsilon_\parallel)$ when $\mu_c \geq 0.2$ eV. The IFC is an ellipse with $\varepsilon_\parallel > 0$, while it will become a hyperbola with $\varepsilon_\parallel < 0$.

To reveal the principle of the zero-reflection-based optical switch, we consider the conditions of $f = 25$ THz and $\alpha = 45°$. For the OFF-state, an elliptic IFC is required, i.e., $\varepsilon_\parallel > 0$. Figures 1(b) and 1(c) suggest that $\mathrm{Re}(\varepsilon_\parallel)$ decreases from positive to negative as μ_c increases, and $\mathrm{Im}(\varepsilon_\parallel)$ is sufficiently small to be neglected when $\mu_c \geq 0.2$ eV. Therefore, we take $\mu_c = 0.2$ eV for the OFF-state. For simplicity, we will use $\varepsilon_\parallel$ instead of $\mathrm{Re}(\varepsilon_\parallel)$ in the following study unless there are additional specifications. As for the ON-state, the zero-reflection-based optical switch requires a hyperbolic IFC with its asymptote perpendicular to the SHM–air interface. This means that the slope of the asymptote should be $k_{\mathrm{asy}} = \pm 1$ and $\varepsilon_\parallel = -\varepsilon_d = -2.2$. According to Fig. 1(b), one can get $\mu_c = 0.82$ eV at $f = 25$ THz for the ON-state.

IFC analysis is used to study the propagation behaviors on the SHM–air interface, as shown in Figs. 2(a) and 2(b). For simplicity, k_x and k_z have been normalized by k_0. In Fig. 2(a), the optical switch is switched off when $\mu_c = 0.2$ eV. Obviously, there exist reflected wave vector $\mathbf{k}_r$ and energy flow $\mathbf{S}_r$, while there is no refracted wave, since the $k_\parallel$ conservation line [i.e., the red dashed line in Fig. 2(a)] does not intersect with the air IFC. In Fig. 2(b), the optical switch is switched on when $\mu_c = 0.82$ eV. Since the normal of the SHM–air interface is parallel to the asymptote of the hyperbolic IFC, one cannot get the reflected wave vector on the IFC of the SHM. Meanwhile, there is no refracted wave either. In other words, one can realize zero reflection and zero refraction simultaneously at the ON-state.

To verify the above predictions, FDTD simulations for a graphene–dielectric structure with actual parameters are shown in Figs. 2(c) and 2(d), which match well with the analysis in Figs. 2(a) and 2(b). For the ON-state in Fig. 2(d), it is hard to see where the energy goes, since most of it is localized near the incident area at the interface. In order to show the propagation behaviors more clearly, a monitor is introduced to record the evolution of the electromagnetic (EM) wave as time elapses. Figure 3 shows snapshots of the evolution movie of the electric field for a Gaussian beam with a finite length of 4850 time steps recorded by the monitor. Obviously, in the case of no reflection and no refraction, the EM wave changes into a surface wave to propagate in the upper-right direction along the air–SHM interface and escape finally. The enlargement inset in Fig. 2(d) also verifies this point. It should be noticed that in order to efficiently couple the EM wave into the structure, the optical switch is designed to be an isosceles right triangle SHM, as shown in Fig. 1(a). The left SHM–air interface with $\alpha = 90°$ is used for coupling light into the device. The transmission for the EM wave incident from the left side is as high as 97% at normal incidence, which is high enough for the application of the device.

It is necessary to discuss the influence of the loss of the dielectric on the optical switch. The loss of the dielectric is characterized by the imaginary part of its permittivity. Figure 4 shows the influence of absorption loss of dielectric layers on the OFF-state ($\mu_c = 0.2$ eV) and ON-state ($\mu_c = 0.82$ eV). Obviously, the larger the loss, the faster it decays with increasing distance. However, the loss has almost no essential influence on the propagation characteristics of the EM wave. For example, when $\varepsilon_d = 2.2 + 0.01i$, it results in a lower reflection only at the OFF-state, but keeps near-zero reflection at the ON-state. Therefore, for simplicity, we assume that the loss of the dielectric is zero for our study.

Further IFC analysis suggests that the optical switch exhibits zero reflection for arbitrary incident angle θ_i from 0° to 90° as long as the frequency and chemical potential are maintained. However, the phenomenon of zero refraction is limited by θ_i. If θ_i decreases continually, a refracted wave vector $\mathbf{k}_r$ satisfying

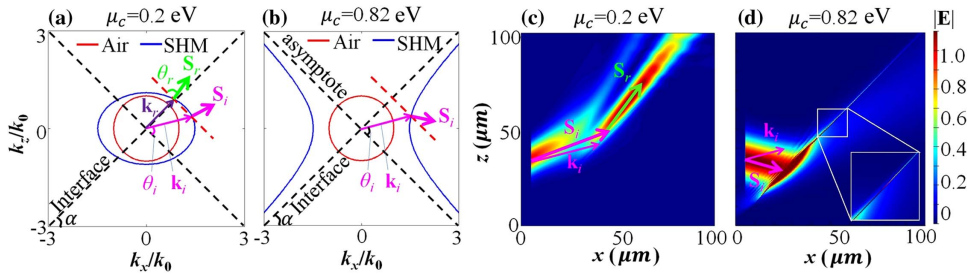

Fig. 2. IFC analysis and simulation results for the optical switch at $\theta_i = 60°$ and $f = 25$ THz. (a), (c) Switch-off state ($\mu_c = 0.2$ eV). (b), (d) Switch-on state ($\mu_c = 0.82$ eV). The inset shows the enlargement of the energy distribution in the denoted square area.

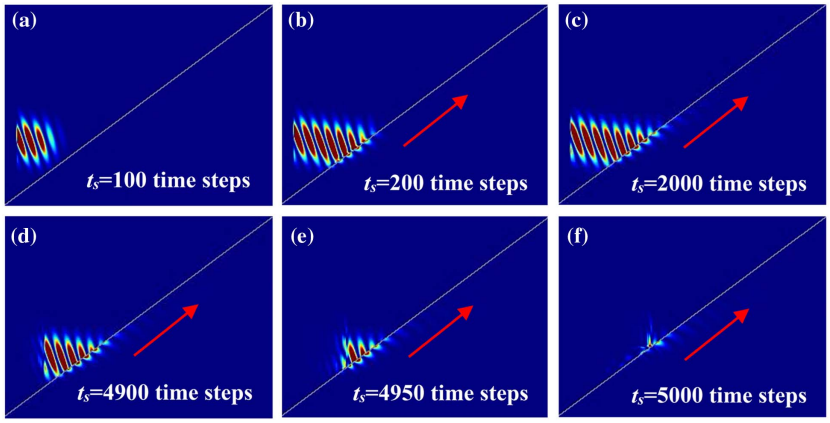

Fig. 3. Snapshots at different time steps for a Gaussian beam with a finite length of time steps. (a) $t_s = 100$ time steps (before touching the interface), (b) $t_s = 200$ time steps (arriving at the interface), and (c) $t_s = 2000$ time steps (stably propagating along the interface). (d)–(f) Three snapshots after the Gaussian beam stops emitting from the source.

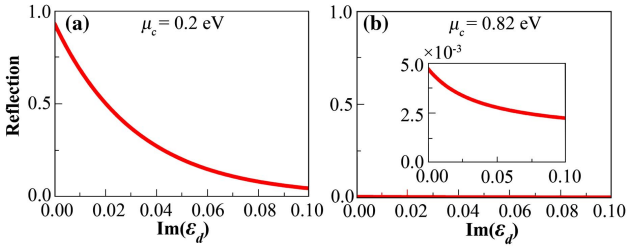

Fig. 4. Influence of absorption loss of dielectric layers on the optical switch. (a) OFF-state ($\mu_c = 0.2$ eV). (b) ON-state ($\mu_c = 0.82$ eV).

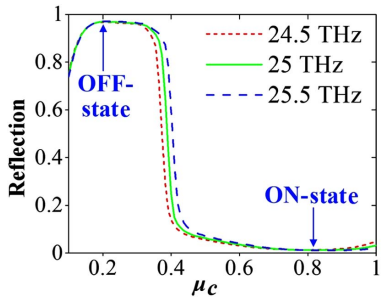

Fig. 5. Variation of reflection with chemical potential for $f = 24.5$ THz, 25 THz, and 25.5 THz.

the $k_{\parallel}$ conservation condition will appear on the air IFC. So there exists a critical incident angle θ_c to decide whether zero refraction appears or not. For $f = 25$ THz and $\mu_c = 0.82$ eV, θ_c is calculated to be 42.3°. However, the refracted light would not disappear completely until $\theta_i = 57°$ in actual FDTD simulations. This is attributed to the width of the waist of the Gaussian light beam. As we know, the smaller the width of the waist, the larger divergence of the Gaussian beam, and thus it results in a wider incident angle range of the Gaussian beam. As for the Gaussian beam with waist width of 10 μm used here, its divergence angle is about 14.4°. Therefore, the refracted light still exists within $42.3° < \theta_i < 57°$ (i.e., $42.3 + 14.4 \approx 57°$), but its intensity weakens as θ_i increases. It should be mentioned that similar phenomena also occur for other sources, including a plane wave, which has an ideal incident angle.

C. Influence of Dispersion on the Designed Optical Switch

The influence of dispersion can be studied by calculating the reflection as a function of μ_c for frequencies around $f = 25$ THz. The incident power in FDTD simulations is set to be unity. Reflection is defined as the energy flowing through the top and left sides of the structure in Fig. 1(a). For $\theta_i = 60°$, the curves of reflection versus μ_c are shown in Fig. 5. For $f = 25$ THz, the reflection reaches zero exactly at $\mu_c = 0.82$ eV, which agrees well with the IFC analysis in Fig. 2(b). Moreover, the reflection curve shifts rightward as f increases; however, the reflection for the OFF-state (or ON-state) at $\mu_c = 0.2$ eV (or 0.82 eV) remains high (>96%) (or near-zero) for $f = 24.5$ THz, 25 THz, and 25.5 THz, meaning that the dispersion of the SHM has almost no influence on the optical switch. What is more, from the viewpoint of applications, such a strict condition for the switch, i.e., single value of chemical potential (0.2/0.82 eV), can be relaxed to a range of chemical potentials, provided that the ratio of reflections at the OFF- and ON-states is high enough. Figure 5 shows that the reflection remains high (>96%) and stable within $0.2 \le \mu_c \le 0.32$ eV for the OFF-state, and it becomes near zero (<1.5%) within $0.77 \le \mu_c \le 0.9$ eV for the ON-state from 24.5 THz to 25.5 THz. The ratio of reflections at the OFF- and ON-states is as high as 96%:1.5% = 64, which is high enough for application. This implies that the optical switch can work in a frequency range by using combinations of μ_c within these two ranges as control parameters, rather than just 0.2/0.82 eV. Such a property provides high tolerance of chemical potential for the optical switch and makes it very convenient in practical applications.

3. DISCUSSION

A. Influence of the Permittivity of Dielectric Sheets and the Period of the Structure

In previous studies, we made default assumptions of $\varepsilon_d = 2.2$ and $d = 0.1$ μm. Actually, these two parameters can efficiently

adjust the working frequency range (f_{min}, f_{max}) of the optical switch. From the discussion in Section 2.B, one can get that for $\alpha = 45°$, the condition of the optical switch is that μ_c should be tuned to guarantee $\varepsilon_\parallel > 0$ (for the OFF-state) or $\varepsilon_\parallel = -\varepsilon_d$ (for the ON-state). Actually, $\varepsilon_\parallel$ is affected not only by μ_c but also by f. In other words, the working frequency range (f_{min}, f_{max}) can be determined by $\varepsilon_\parallel$ and μ_c together.

First, we discuss the lower limit f_{min}. Figures 1(b) and 1(c) show that $\mathrm{Re}(\varepsilon_\parallel)$ increases with decreasing μ_c; however, $\mathrm{Im}(\varepsilon_\parallel)$ increases rapidly when μ_c decreases from 0.2 eV to 0 eV, so $\mu_c = 0.2$ eV is the minimum available value. On the other hand, $\mathrm{Re}(\varepsilon_\parallel)$ decreases from positive to negative as f decreases. Obviously, there exists a frequency threshold where $\mathrm{Re}(\varepsilon_\parallel) = 0$ [or $\varepsilon_\parallel = 0$ for simplicity due to negligible $\mathrm{Im}(\varepsilon_\parallel)$]. Since the OFF-state requires $\varepsilon_\parallel > 0$, this frequency threshold is f_{min}. In a word, f_{min} is determined by $\mu_c = 0.2$ eV and $\varepsilon_\parallel = 0$ together. As for f_{max}, Fig. 1(b) shows that with increasing f, $\mathrm{Re}(\varepsilon_\parallel)$ increases, and a larger μ_c is required to maintain $\varepsilon_\parallel = -\varepsilon_d = -2.2$ for the ON-state. However, μ_c cannot increase indefinitely. So we assume $\mu_c = 0.9$ eV to be the maximum available value, since in this case, the reflection is still near zero as discussed in Section 2.C. Therefore, f_{max} is determined by $\mu_c = 0.9$ eV and $\varepsilon_\parallel = -\varepsilon_d$.

It is convenient to obtain f_{min} and f_{max} from the μ_c-f curves to study the influence of ε_d and d. We first study the influence of ε_d while keeping $d = 0.1$ μm. The relations of μ_c versus f satisfying $\varepsilon_\parallel = 0$ and $\varepsilon_\parallel = -\varepsilon_d$ for different ε_d are presented in Figs. 6(a) and 6(b), respectively. f_{min} and f_{max} are determined by the intersections of μ_c-f curves and the two dashed horizontal lines located at $\mu_c = 0.2$ eV and 0.9 eV, respectively. Obviously, both f_{min} and f_{max} decrease as ε_d increases, and the absolute bandwidth $\Delta f = f_{max} - f_{min}$ decreases, too. In other words, the smaller the ε_d, the wider the bandwidth. Specifically, the working frequency ranges, i.e., (f_{min}, f_{max}), are (24.8, 38.7) THz, (17.1, 26.1) THz, (14.8, 22.4) THz, (12.7, 19.3) THz, and (11.5, 17.3) THz for $\varepsilon_d = 1$, 2.2, 3, 4, and 5, respectively. For the designed optical switch with $\varepsilon_d = 2.2$ and $d = 0.1$ μm in Section 2, it can work in a broad frequency range from 17.1 THz to 26.2 THz.

Then we study the influence of d while keeping ε_d as a constant. Without loss of generality, we keep $\varepsilon_d = 1$, though it is impossible to select air ($\varepsilon_d = 1$) to construct a real SHM. Figures 6(c) and 6(d) show the μ_c-f curves satisfying conditions of $\varepsilon_\parallel = 0$ and $\varepsilon_\parallel = -1$, respectively, for different d. Through similar analysis, one can find that no matter whether $\varepsilon_\parallel = 0$ or −1, all f-μ_c curves shift rightward as d decreases, meaning that both f_{min} and f_{max} increase with decreasing d. Specifically, the working frequency ranges are (48.2, 85.4) THz, (31.2, 49.7) THz, (24.8, 38.7) THz, (21.6, 32.7) THz, and (19.1, 28.9) THz for $d = 0.02$ μm, 0.06 μm, 0.1 μm, 0.14 μm, and 0.18 μm, respectively. Apparently, the absolute bandwidth $\Delta f = f_{max} - f_{min}$ decreases significantly as d increases (from 37.2 THz to 9.8 THz when d increases from 0.02 μm to 0.18 μm).

B. Influence of the Slanted Angle α on the Zero Reflection Effect

So far, we have assumed $\alpha = 45°$. Actually, no matter what α is, it is always possible to realize zero reflection provided that the asymptote of the hyperbolic IFC is perpendicular to the interface whose slope is $k_\alpha = \tan\alpha$. For the hyperbola described by Eq. (4), the slope of one asymptote is $k_{asy} = -(-\varepsilon_\parallel/\varepsilon_\perp)^{1/2}$ ($\varepsilon_\parallel < 0$). So we get the required $\varepsilon_\parallel$ described by α from $k_\alpha \cdot k_{asy} = -1$ as

$$\varepsilon_\parallel = -\frac{\varepsilon_\perp}{\tan^2\alpha}. \tag{5}$$

For parameters of $\varepsilon_d = 2.2$ and $d = 0.1$ μm, the required $\varepsilon_\parallel$ for zero reflection are −16.6, −2.2, −0.73, and −0.07 when $\alpha = 20°, 45°, 60°$, and 80°, respectively. For these special values of $\varepsilon_\parallel$, the relations of μ_c versus f are shown in Fig. 7(a), which can be used to determine the upper limit f_{max}. When α increases, the corresponding μ_c-f curve shifts rightward, leading to a larger f_{max}. The upper limits f_{max} for $\alpha = 20°, 45°, 60°$, and 80° are 12.6 THz, 26.2 THz, 32 THz, and 36.3 THz, respectively, as denoted by the dashed line at $\mu_c = 0.9$ eV in Fig. 7(a). On the other hand, since the required μ_c for OFF-state still remains at 0.2 eV, the lower limit f_{min} is still 17.1 THz. Therefore, it is an effective way to enlarge the working bandwidth by increasing the slanted angle α.

We further discuss the effective incident angle range ($\theta_{i\,min}$, $\theta_{i\,max}$). One asymptote of the hyperbolic IFC perpendicular to the SHM–air interface has a slope of $k_{asy} = -1/k_\alpha = -1/\tan\alpha$. The SHM supports wave vectors $\mathbf{k}_i$ only within these two asymptotes, as shown in Fig. 7(b) where the hyperbolic IFC at $f = 25$ THz for the case of $\alpha = 80°$ and $\varepsilon_\parallel = -0.07$ is drawn. Obviously, $\theta_{i\,min}$ is 0°. As for $\theta_{i\,max}$, if the angle between the two asymptotes is less than 90°, $\theta_{i\,max} = 2\arctan(1/\tan\alpha) = 2(90° - \alpha)$; otherwise, $\theta_{i\,max} = 90°$ because an incident angle cannot be larger than 90°. The curve of $\theta_{i\,max}$ versus α is shown in Fig. 7(c). Obviously, $\theta_{i\,max}$ decreases linearly when $\alpha > 45°$. Usually, f_{max} is desired to be

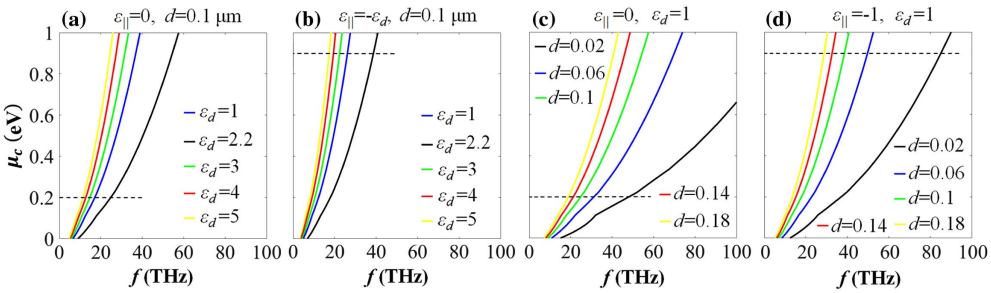

Fig. 6. μ_c-f curves with different parameter conditions: (a) $\varepsilon_\parallel = 0$, $d = 0.1$ μm; (b) $\varepsilon_\parallel = -\varepsilon_d$, $d = 0.1$ μm; (c) $\varepsilon_\parallel = 0$, $\varepsilon_d = 1$; (d) $\varepsilon_\parallel = -1$, $\varepsilon_d = 1$. The dashed lines indicate $\mu_c = 0.2$ eV and 0.9 eV, respectively.

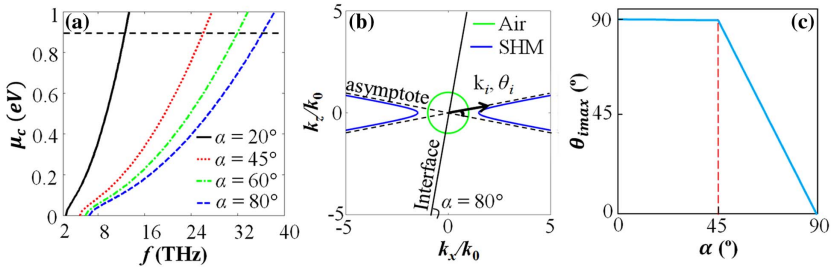

Fig. 7. (a) μ_c-f curves for $\alpha = 20°, 45°, 60°$, and 80°. (b) IFC at $f = 25$ THz for $\alpha = 80°$ and $\varepsilon_{\parallel} = -0.07$. (c) Dependence of maximal incident angle $\theta_{i\,\max}$ on the slanted angle α.

as large as possible, and at the same time the SHM should support arbitrary θ_i between 0° and 90°. Therefore, $\alpha = 45°$ is the optimal selection for the SHM–air interface.

4. CONCLUSION

In conclusion, we have realized the zero reflection effect in a graphene–dielectric SHM and demonstrated an all-angle compact optical switch. The IFC of this SHM can be conveniently switched between an ellipse and a hyperbola by tuning the chemical potential. In particular, when the asymptote of the hyperbolic IFC is perpendicular to the SHM–air interface, zero reflection can be realized. Based on these unique properties, an all-angle optical switch is proposed. It can work at high reflection (>96%) (OFF-state) over $0.2 \le \mu_c \le 0.32$ eV and near-zero reflection (ON-state) over $0.77 \le \mu_c \le 0.9$ eV, providing high tolerance of chemical potential in practical applications. Moreover, its working bandwidth can be effectively adjusted by permittivity of the dielectric, period of the structure, and the slanted angle of the SHM–air interface. These results hold great potential in many fields, such as data storage, beam steering, and THz wave sensing, as well as integrated photonic circuits.

Funding. National Natural Science Foundation of China (NSFC) (11504114, 11434017); National Key R&D Program of China (2018YFA 0306200); Science and Technology Program of Guangzhou, China; SRP of South China University of Technology.

REFERENCES

1. D. R. Smith, J. B. Pendry, and M. C. K. Wiltshire, "Metamaterials and negative refractive index," Science **305**, 788–792 (2004).
2. J. B. Pendry, D. Schurig, and D. R. Smith, "Controlling electromagnetic fields," Science **312**, 1780–1782 (2006).
3. Q. Zhao, T. Zhou, T. Wang, W. Liu, J. Liu, T. Yu, Q. Liao, and N. Liu, "Active control of near-field radiative heat transfer between graphene-covered metamaterials," J. Phys. D **50**, 145101 (2017).
4. D. R. Smith and D. Schurig, "Electromagnetic wave propagation in media with indefinite permittivity and permeability tensors," Phys. Rev. Lett. **90**, 077405 (2003).
5. Y. Guo, W. Newman, C. L. Cortes, and Z. Jacob, "Applications of hyperbolic metamaterial substrates," Adv. OptoElectron. **2012**, 452502 (2012).
6. K. V. Sreekanth, A. De Luca, and G. Strangi, "Negative refraction in graphene-based hyperbolic metamaterials," Appl. Phys. Lett. **103**, 023107 (2013).
7. J. Hoffman, L. Alekseyev, S. S. Howard, K. J. Franz, D. Wasserman, V. A. Podolskiy, E. E. Narimanov, D. L. Sivco, and C. Gmachl, "Negative refraction in semiconductor metamaterials," Nat. Mater. **6**, 946–950 (2007).
8. C. Argyropoulos, N. M. Estakhri, F. Monticone, and A. Alù, "Negative refraction, gain and nonlinear effects in hyperbolic metamaterials," Opt. Express **21**, 15037–15047 (2013).
9. A. D. Neira, G. A. Wurtz, and A. V. Zayats, "Superluminal and stopped light due to mode coupling in confined hyperbolic metamaterial waveguides," Sci. Rep. **5**, 17678 (2015).
10. S. H. Liang, C. H. Jiang, Z. Q. Yang, D. C. Li, W. D. Zhang, T. Mei, and D. W. Zhang, "Plasmonic slow light waveguide with hyperbolic metamaterials claddings," J. Opt. **20**, 065001 (2018).
11. T. F. Li, V. Nagai, D. H. Gracias, and J. B. Khurgin, "Limits of imaging with multilayer hyperbolic metamaterials," Opt. Express **25**, 13588–13601 (2017).
12. D. Lu, J. J. Kan, E. E. Fullerton, and Z. W. Liu, "Enhancing spontaneous emission rates of molecules using nanopatterned multilayer hyperbolic metamaterials," Nat. Nanotechnol. **9**, 48–53 (2014).
13. K. J. Lee, Y. U. Lee, S. J. Kim, and P. André, "Hyperbolic dispersion dominant regime identified through spontaneous emission variations near metamaterial interfaces," Adv. Mater. Interfaces **5**, 1701629 (2018).
14. T. A. Morgado, S. I. Maslovski, and M. G. Silveirinha, "Ultrahigh Casimir interaction torque in nanowire systems," Opt. Express **21**, 14943–14955 (2013).
15. M. Kim, S. Kim, and S. Kim, "Optical bistability based on hyperbolic metamaterials," Opt. Express **26**, 11620–11632 (2018).
16. X. Li, Z. X. Liang, X. H. Liu, X. Y. Jiang, and J. Zi, "All-angle zero reflection at metamaterial surfaces," Appl. Phys. Lett. **93**, 171111 (2008).
17. W. Li, Z. Liu, X. Zhang, and X. Y. Jiang, "Switchable hyperbolic metamaterials with magnetic control," Appl. Phys. Lett. **100**, 161108 (2012).
18. K. S. Novoselov, A. K. Geim, S. V. Morozov, D. Jiang, Y. Zhang, S. V. Dubonos, I. V. Grigorieva, and A. A. Firsov, "Electric field effect in atomically thin carbon films," Science **306**, 666–669 (2004).
19. G. W. Hanson, "Dyadic Green's functions and guided surface waves for a surface conductivity model of graphene," J. Appl. Phys. **103**, 064302 (2008).
20. A. Vakil and N. Engheta, "Transformation optics using graphene," Science **332**, 1291–1294 (2011).
21. H. Deng, F. Ye, B. A. Malomed, X. Chen, and N. C. Panoiu, "Optically and electrically tunable Dirac points and Zitterbewegung in graphene-based photonic superlattices," Phys. Rev. B **91**, 201402 (2015).
22. H. Deng, X. Chen, B. A. Malomed, N. C. Panoiu, and F. Ye, "Tunability and robustness of Dirac points of photonic nanostructures," IEEE J. Sel. Top. Quantum Electron. **22**, 98–106 (2016).
23. Y. C. Chang, C. H. Liu, C. H. Liu, S. Zhang, S. R. Marder, E. E. Narimanov, Z. Zhong, and T. B. Norris, "Realization of mid-infrared graphene hyperbolic metamaterials," Nat. Commun. **7**, 10568 (2016).
24. T. Gric and O. Hess, "Tunable surface waves at the interface separating different graphene-dielectric composite hyperbolic metamaterials," Opt. Express **25**, 11466–11476 (2017).
25. B. Zhu, G. Ren, S. Zheng, Z. Lin, and S. Jian, "Nanoscale dielectric-graphene-dielectric tunable infrared waveguide with ultrahigh refractive indices," Opt. Express **21**, 17089–17096 (2013).

26. I. V. Iorsh, I. S. Mukhin, I. V. Shadrivov, P. A. Belov, and Y. S. Kivshar, "Hyperbolic metamaterials based on multilayer graphene structures," Phys. Rev. B **87**, 075416 (2013).
27. H. G. Liu, P. G. Liu, L. A. Bian, C. X. Liu, Q. H. Zhou, and Y. W. Chen, "Electrically tunable terahertz metamaterials based on graphene stacks array," Superlattices Microstruct. **112**, 470–479 (2017).
28. B. Janaszek, A. Tyszka-Zawadzka, and P. Szczepański, "Tunable graphene-based hyperbolic metamaterial operating in SCLU telecom bands," Opt. Express **24**, 24129–24136 (2016).
29. M. Shoaei, M. K. Moravvej-Farshi, and L. Yousefi, "Nanostructured graphene-based hyperbolic metamaterial performing as a wide-angle near infrared electro-optical switch," Appl. Opt. **54**, 1206–1211 (2015).
30. M. A. K. Othman, C. Guclu, and F. Capolino, "Graphene-dielectric composite metamaterials: evolution from elliptic to hyperbolic wave-vector dispersion and the transverse epsilon-near-zero condition," J. Nanophoton. **7**, 073089 (2013).
31. H. N. S. Krishnamoorthy, Z. Jacob, E. Narimanov, I. Kretzschmar, and V. M. Menon, "Topological transitions in metamaterials," Science **336**, 205–209 (2012).
32. S. Campione, T. S. Luk, S. Liu, and M. B. Sinclair, "Optical properties of transiently-excited semiconductor hyperbolic metamaterials," Opt. Mater. Express **5**, 2385–2394 (2015).
33. F. H. Shi, Y. H. Chen, P. Han, and P. Tassin, "Broadband, spectrally flat, graphene-based terahertz modulators," Small **11**, 6044–6050 (2015).
34. W. G. Liu, B. Hu, Z. D. Huang, H. Y. Guan, H. T. Li, X. K. Wang, Y. Zhang, H. X. Yin, X. L. Xiong, J. Liu, and Y. T. Wang, "Graphene-enabled electrically controlled terahertz meta-lens," Photon. Res. **6**, 703–708 (2018).
35. C. Guclu, S. Campione, and F. Capolino, "Hyperbolic metamaterial as super absorber for scattered fields generated at its surface," Phys. Rev. B **86**, 205130 (2012).
36. Y. Zhang, Y. Shi, and C. H. Liang, "Broadband tunable graphene-based metamaterial absorber," Opt. Mater. Express **6**, 3036–3044 (2016).
37. Y. T. Zhao, B. A. Wu, B. J. Huang, and Q. A. Cheng, "Switchable broadband terahertz absorber/reflector enabled by hybrid graphene-gold metasurface," Opt. Express **25**, 7161–7169 (2017).
38. Y. Shi and Y. Zhang, "Generation of wideband tunable orbital angular momentum vortex waves using graphene metamaterial reflectarray," IEEE Access **6**, 5341–5347 (2018).
39. Z. Li, W. Y. Liang, and W. H. Chen, "Switchable hyperbolic metamaterials based on the graphene-dielectric stacking structure and optical switches design," Europhys. Lett. **120**, 37001 (2017).
40. H. N. S. Krishnamoorthy, B. Gholipour, N. I. Zheludev, and C. Soci, "A non-volatile chalcogenide switchable hyperbolic metamaterial," Adv. Opt. Mater. **6**, 1800332 (2018).
41. M. Shoaei, M. K. Moravvej-Farshi, and L. Yousefi, "All-optical switching of nonlinear hyperbolic metamaterials in visible and near-infrared regions," J. Opt. Soc. Am. B **32**, 2358–2365 (2015).
42. J. Qin, H. M. Dong, K. Han, and X. F. Wang, "Ultrafast dynamic optical properties of graphene," Acta Phys. Sin. **64**, 237801 (2015).
43. V. P. Gusynin, S. G. Sharapov, and J. P. Carbotte, "Magneto-optical conductivity in graphene," J. Phys. Condens. Matter **19**, 026222 (2007).
44. M. A. K. Othman, C. Guclu, and F. Capolino, "Graphene-based tunable hyperbolic metamaterials and enhanced near-field absorption," Opt. Express **21**, 7614–7632 (2013).